



Silicate Weathering in the Semi-Arid Southern Pyrenees During the PETM: Lithium Isotope Evidence

Rocio Jaimes-Gutierrez¹, Marine Prieur¹, David J. Wilson², Philip A.E. Pogge von Strandmann^{2,3}, Emmanuelle Pucéat⁴, Thierry Adatte⁵, Jorge E. Spangenberg⁶, Sébastien Castelltort¹

¹ Department of Earth Sciences, University of Geneva, Rue des Maraîchers 13, 1205, Geneva, Switzerland

² London Geochemistry and Isotope Centre (LOGIC), Institute of Earth and Planetary Sciences, University College London and Birkbeck, University of London, Gower Street, London WC1E 6BT, UK

³ Institute of Geosciences, Johannes Gutenberg University Mainz, Mainz, Germany

⁴ Biogéosciences Dijon, Université Bourgogne Franche – Comté, UMR CNRS 6282, Dijon, France.

⁵ Institute of Earth Sciences, Géopolis, University of Lausanne, 1015 Lausanne, Switzerland

⁶ Institute of Earth Surface Dynamics, Géopolis, University of Lausanne, 1015 Lausanne, Switzerland

Correspondence to: Rocio Jaimes-Gutierrez, Rocio.JaimesGutierrez@unige.ch

Abstract

The Palaeocene-Eocene Thermal Maximum (PETM), a hyperthermal event ~56 Ma ago, allows the Earth system response to abrupt climate change to be explored. Recent investigations link the PETM with a negative lithium isotope ($\delta^7\text{Li}$) excursion, interpreted as an increase in continental silicate weathering fluxes, which can regulate Earth's surface temperature over geological timescales. However, the silicate weathering response under different climatic regimes has yet to be constrained. Here we aim to address the chemical weathering response to the PETM in the semi-arid Southern Pyrenees, and to explore how different archives (i.e., clays and carbonate nodules) record the weathering changes.

We investigated two continental sections in the southern Pyrenees. In the Esplugafreda section, we measured $\delta^7\text{Li}$ values as a silicate weathering proxy and ϵ_{Nd} values as a provenance proxy in the clay minerals. In the Rin section, we characterised the PETM locally by analysing $\delta^{13}\text{C}$ values in organic matter and examined the clay mineralogy in the paleosols, as well as measuring $\delta^7\text{Li}$ values in clays and carbonate nodules to trace silicate weathering. In the Esplugafreda section, we observe temporally stable ϵ_{Nd} values, while the $\delta^7\text{Li}_{\text{clay}}$ record shows two small positive excursions, one during the Pre-Onset Excursion (~0.7‰) and a second during the body of the PETM (~0.8‰). In the Rin section, the PETM is characterised by a negative carbon isotope excursion of 2.8‰. The clays consist mostly of illite/smectite, illite, and kaolinite, consistent with a seasonal climate in the region, and we find a positive $\delta^7\text{Li}_{\text{clay}}$ excursion of ~0.8‰.

The combined $\delta^7\text{Li}_{\text{clays}}$ and ϵ_{Nd} records indicate increased clay formation and increased silicate weathering fluxes in the semi-arid Pyrenees, while the sediment provenance was stable. The $\delta^7\text{Li}$ values in the carbonate nodules indicate more variability, potentially due to clay contamination. Constrained by the bedrock type of dominantly reworked sediments and the seasonal precipitation regime, the initially low weathering rate, despite a comparatively high weathering intensity, evolved towards a higher weathering rate with enhanced erosion during the PETM.

Short Summary

This study examines how weathering in the Southern Pyrenees responded to a significant global warming event that occurred 56 million years ago. We found that changes in rainfall and erosion significantly influenced how minerals break down, and that the weathering response evolved from the continental interior to the marine environment. These results highlight regional variations in Earth's surface response to climatic perturbations and the processes at play in response to global warming.



1. Introduction

Continental silicate weathering is a critical feedback mechanism that stabilises Earth's climate over geological timescales by regulating atmospheric CO₂ through the long-term carbon cycle (Walker et al., 1981; Raymo and Ruddiman, 1992; Maher and Von Blanckenburg, 2023). Through the breakdown of silicate minerals, the transport of cations in river systems, and the precipitation and burial of carbonates in the ocean, silicate weathering sequesters atmospheric CO₂, acting as a natural climate thermostat. Understanding how this process responds to abrupt climate change is essential for evaluating its capacity to modulate carbon fluxes under a range of future warming scenarios.

The Palaeocene-Eocene Thermal Maximum (PETM), a hyperthermal event ~56 Ma ago, was related to the rapid release of greenhouse gases that triggered a 5–8 °C global temperature increase over a geologically brief interval (Kennett and Stott, 1991; Dickens et al., 1995; Zachos et al., 2003, 2008; Westerhold et al., 2009; McInerney and Wing, 2011). Global records from the PETM suggest increases in silicate weathering fluxes (e.g., Hessler et al., 2017; Pogge von Strandmann et al., 2021), while some local records have been interpreted to show increased weathering intensity (e.g., Ramos et al., 2022; Chen et al., 2023), underscoring its potential to buffer atmospheric CO₂ during extreme warming events. In the context of modern anthropogenic warming, these insights are crucial for understanding the capacity of natural systems to mitigate rising CO₂ levels (Zeebe et al., 2016; Carmichael et al., 2017 and references therein).

In mid-latitude records, a range of sedimentological, geochemical, and mineralogical proxies suggest that the PETM resulted in a hydrological perturbation with episodic extreme rainfall events, increased seasonality, and aridification, leading to a loss of vegetation, extreme flooding, and enhanced channel mobility (Schmitz et al., 2001; Schmitz and Pujalte, 2007; Carmichael et al., 2017; Chen et al., 2018; Rush et al., 2021; Barefoot et al., 2022; Vimpere et al., 2023). These changes were particularly pronounced in semi-arid regions such as the Southern Pyrenees (~35°N paleolatitude, **Fig. 1**), where sedimentary records document hydrological seasonality, enhanced erosion, and increased sediment transport (Schmitz and Pujalte, 2007; Pujalte et al., 2015; Chen et al., 2018; Rush et al., 2021; Prieur et al., 2024, 2025; Jaimes-Gutierrez et al., 2024).

The Southern Pyrenees (**Fig. 1**) offer an exceptional setting for investigating climate-driven weathering dynamics. This region experienced tectonic quiescence during the PETM (Rosenbaum et al., 2002), allowing for the isolation of the effects of climate and hydrology on weathering. Sedimentary records indicate enhanced hydrological seasonality and increased runoff, consistent with amplified denudation rates during this interval (Schmitz and Pujalte, 2007; Pujalte et al., 2015; Rush et al., 2021). In this study, we use lithium isotopes ($\delta^7\text{Li}$) as a proxy for silicate weathering and neodymium isotopes (ϵ_{Nd}) as a tracer for sediment provenance, in order to quantify the weathering responses in the Southern Pyrenees and to assess their regional contribution to CO₂ regulation during the PETM.

We focus on two continental floodplain sections to answer two primary questions: (i) What was the chemical weathering response to the PETM in the semi-arid Southern Pyrenees? (ii) How do different sedimentary archives, such as clays and carbonate nodules, record the weathering changes? In the Esplugafreda section, we measured lithium isotopes ($\delta^7\text{Li}$) in clay minerals as a weathering proxy, together with neodymium isotopes in two clay size fractions (ϵ_{Nd}) to determine sediment provenance. In the Rin section, we characterised the PETM locally through $\delta^{13}\text{C}$ measurements in organic matter, and analysed the clay mineralogy of paleosols, and $\delta^7\text{Li}$ values in both clays and carbonate nodules. These geochemical and mineralogical datasets allow us to reconstruct weathering dynamics in the region and to assess how they compare with existing globally-distributed records of PETM weathering (Pogge von Strandmann et al., 2021; Ramos et al., 2022; Chen et al., 2023).

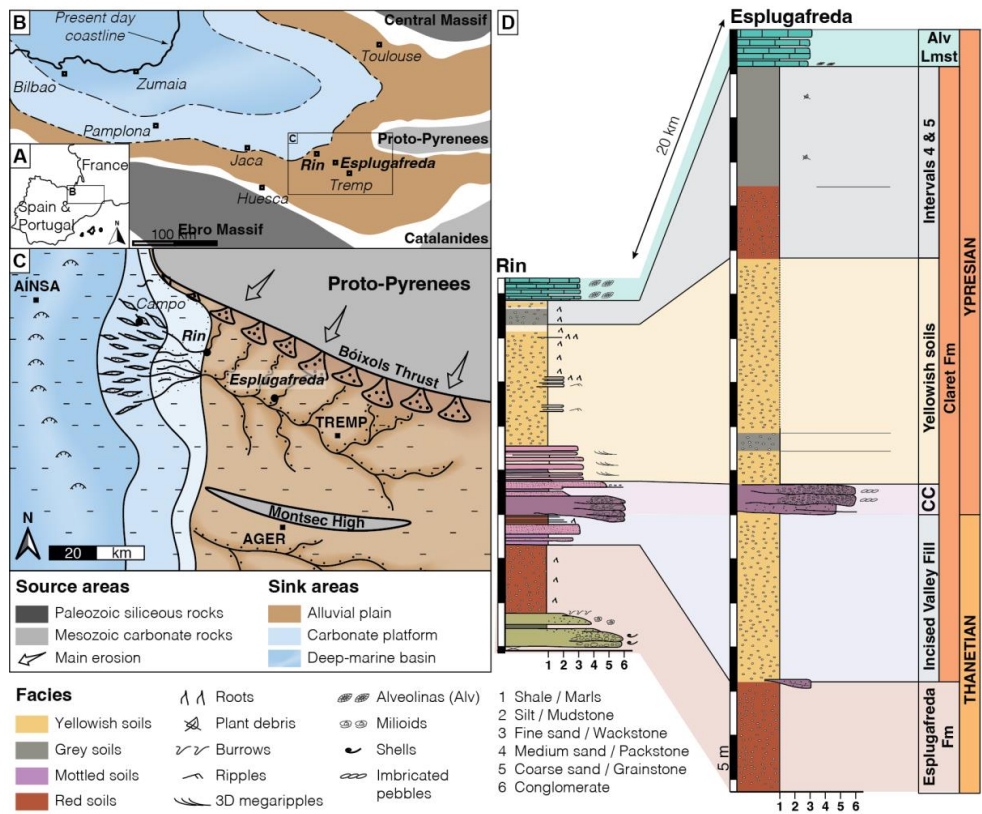


Figure 1. (A) Location map. (B) Palaeogeography of the Tremp-Graus Basin during the late Palaeocene, modified after Jaimes-Gutierrez et al. (2024) and references therein. (C) Sediment routing system during the late Palaeocene, with the floodplain Esplugafreda section and the more coastal Rin section, at the marine-continent transition, modified from Prieur et al. (2025). (D) Stratigraphy and correlation between the Esplugafreda and Rin terrestrial sections. CC, Claret Conglomerate.

1.1. Silicate weathering as Earth's surface thermostat

Silicate weathering rates are influenced by climate (Dessert et al., 2003; West et al., 2005), vegetation (Moulton et al., 2000; Porder, 2019), lithology (Dessert et al., 2003; Caves et al., 2016; Murray and Jagoutz, 2024), and regolith properties (Kump and Arthur, 1997; Caves Rugenstein et al., 2019). Weathering is driven by the availability of fresh mineral surfaces, reactive fluids, and dissolution kinetics (Riebe et al., 2004; Bufer et al., 2021; Maher and Von Blanckenburg, 2023). Denudation ($D = \text{erosion rate } [E] + \text{silicate weathering } [W]$) links surface processes to the carbon cycle because erosion supplies fresh minerals, enhancing CO_2 sequestration through chemical weathering (Gaillardet et al., 1999; Riebe et al., 2004; Anderson et al., 2007; Hilton, 2023). However, weathering efficiency peaks at intermediate erosion rates, while extremely thin or thick soils reduce weathering fluxes (Gabet and Mudd, 2009; Dixon and Von Blanckenburg, 2012; Bufer et al., 2024).

Two end-member regimes can be used to describe chemical weathering dynamics. In supply-limited regimes, mature soils dominated by secondary clays shield bedrock, limiting fresh mineral exposure and resulting in low weathering rates (Goddéris et al., 2008). In kinetically-limited regimes, which are typical of high-relief areas with thin soils, weathering rates are controlled by mineral dissolution kinetics and increase with erosion (Kump et al., 2000; Riebe et al., 2004; West et al., 2005). Investigating how climate and erosion interact to shape these regimes under hyperthermal events such as the PETM is thus essential for understanding the weathering mechanisms and rates underpinning Earth's carbon cycle feedbacks in a warming climate.



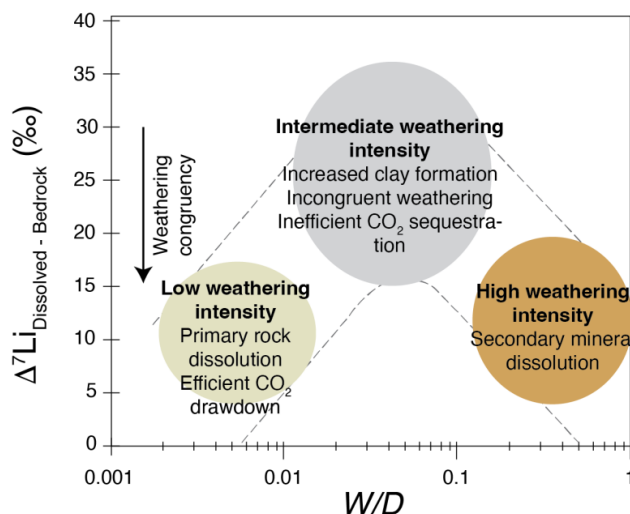
1.2. Lithium isotopes as a chemical weathering tracer

Secondary clay minerals, which form as a by-product of primary silicate rock dissolution, preferentially incorporate ^6Li over ^7Li , which leads to clays that are isotopically light and waters that are isotopically heavy (e.g., Pogge von Strandmann et al., 2020). As weathering progresses, both the water and the clays that precipitate from it become isotopically heavier, with the $\delta^7\text{Li}$ value of the water and soil being linked by an approximately constant fractionation factor (Pogge von Strandmann et al., 2021a). Measuring $\delta^7\text{Li}$ values in detrital (clay) and carbonate archives therefore allows past weathering regimes to be reconstructed. Because carbonate weathering has a minimal influence on riverine Li concentrations, even in carbonate-dominated terrains, $\delta^7\text{Li}$ values reflect silicate weathering processes (Kisakürek et al., 2005). Hence, lithium isotopes have become widely applied as a proxy for tracking clay mineral formation, and thereby tracing silicate weathering intensity changes, both in modern systems (e.g., Dellinger et al., 2015, 2017; Pogge von Strandmann et al., 2023) and during past geological events (e.g., Misra and Froelich, 2012; Pogge von Strandmann et al., 2013, 2021; Ramos et al., 2022; Jones et al., 2023).

Weathering congruency, which represents the balance between primary mineral dissolution and secondary clay mineral formation, determines the $\delta^7\text{Li}$ composition of river waters and sediments (Dellinger et al., 2015; Zhang et al., 2022 and references therein). In modern rivers, lithium isotopes in both the solution and the associated clays are related to the silicate weathering intensity (W/D) via a “boomerang” shape (Fig. 2). In rapidly eroding regions with low W/D, congruent weathering results in minimal isotopic fractionation, because clay formation is relatively low (Fig. 3). In contrast, incongruent weathering in soil-mantled environments with moderate W/D, such as floodplains with high clay formation, yields both clays and waters with higher $\delta^7\text{Li}$ values (Fig. 3). Finally, in supply-limited regimes with high W/D, such as rainforests, there is no remaining primary rock material to weather, so pre-formed clays are re-dissolved, which drives solution $\delta^7\text{Li}$ to low values, but with a very low weathering flux (e.g., Dellinger et al., 2015). Clays take up their Li from solution with an approximately constant fractionation factor, so they are also expected to mimic this boomerang curve (Dellinger et al., 2017; Pogge von Strandmann et al., 2023; Ramos et al., 2024). However, we note that under high W/D conditions, existing clays largely re-dissolve and there is minimal clay neoformation, so clays in such a regime must largely be inherited from elsewhere.

In bulk river sediment samples, only part of this boomerang trend is typically observed because of mixing of the neoformed clays with primary silicate material, especially at low W/D conditions (Dellinger et al., 2017). Therefore, continental and marine detrital records may need to be interpreted differently (e.g., Pogge von Strandmann et al., 2021; Ramos et al., 2022, 2024; Jones et al., 2023). Because fewer of the coarser-grained primary minerals carried in rivers are expected to be transported into offshore sites, the clay weathering signal may generally be recorded more clearly in marine sites. However, such biases resulting from mixing with primary silicate grains in bulk sediment samples can potentially be significantly reduced by analysing the clay size fraction ($<2\ \mu\text{m}$).

Finally, we note that lithium isotopes can also be fractionated by direct climatic fluctuations. For example, temperature (Vigier et al., 2008; Li and West, 2014) and hydrological controls (Zhang et al., 2022) have both been found to influence the $\delta^7\text{Li}$ composition of river water, and consequently the composition of the sedimentary archives that form in equilibrium with them (Pogge von Strandmann et al., 2023). In particular, riverine dissolved $\delta^7\text{Li}$ values have been shown to have a negative correlation with runoff, because it controls the water-rock residence time that affects clay formation, with the dry season exhibiting enhanced clay formation and higher $\delta^7\text{Li}$ values than the wet season (Wilson et al., 2021; Zhang et al., 2022).



164
165 **Figure 2.** Large-river dissolved lithium isotope composition ($\delta^7\text{Li}_{\text{dissolved}}$) corrected for bedrock composition
166 ($\Delta^7\text{Li}_{\text{dissolved-bedrock}}$) plotted versus weathering intensity (W/D). Modified from Dellinger et al. (2015) and references
167 therein.

168
169 During the PETM, Pogge von Strandmann et al. (2021) documented a $\sim 3\text{‰}$ negative $\delta^7\text{Li}$ excursion in several
170 marine carbonate sections, indicating globally enhanced weathering fluxes (50–60%) and erosion rates (2–3x),
171 and a shift to an overall lower weathering intensity regime. On a regional scale, Ramos et al. (2022) reported a
172 rapid, sustained increase in silicate weathering intensity in the Bighorn Basin floodplains that was attributed to
173 seasonal hydrological variability. Similarly, Chen et al. (2023) identified a $\sim 100\%$ increase in silicate weathering
174 intensity in the Nanyang Basin. These studies highlight the roles of local hydrology, lithology, and erosion in
175 shaping regional weathering responses and the associated $\delta^7\text{Li}$ changes. However, they also reveal significant
176 gaps in our understanding of how regional processes integrate into driving global $\delta^7\text{Li}$ records and carbon cycle
177 feedbacks. Notably, discrepancies between the proposed increases in weathering intensity at a regional scale
178 (Ramos et al., 2022; Chen et al., 2023) and the inferred decrease at a global scale (Pogge von Strandmann et al.,
179 2021) require further assessment of how regional climatic and geological controls translate into weathering
180 responses.
181

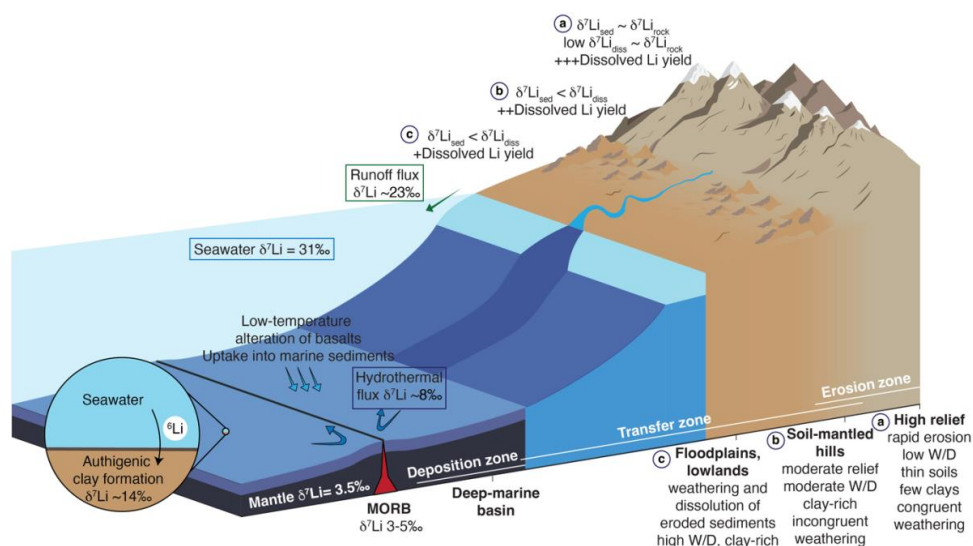


Figure 3. Processes determining the lithium isotope composition of bulk sediments ($\delta^7\text{Li}_{\text{sed}}$) and lithium flux along a sediment routing system from source to sink in relation to denudation. The weathering intensity (W) expresses the relative share of weathering (W) over denudation (D), where $D = W + E$ (erosion). Modified from Tofelde et al. (2021), Pogge von Strandmann et al. (2021a), and Bufer et al. (2024).

To address these gaps, we focused on the silicate weathering response to the PETM climatic perturbation in two sections of the Southern Pyrenees (Espugafreda and Rin, **Fig. 1**). With its semi-arid climate, seasonal precipitation, and relatively unreactive lithologies comprising reworked sediments and significant carbonate content (e.g., Eichenseer, 1988; Eichenseer and Luterbacher, 1992; Gómez-Gras et al., 2016), this setting represents a contrasting regional weathering regime to previous PETM studies. Our results contribute to understanding how floodplain paleosols, which are often overlooked in global weathering studies, respond to climatic perturbations, with broader implications for the recovery of Earth's climate system after significant warming events.

2. Geological context

The Pyrenees formed as a result of convergence between the Iberian and European plates, a process that initiated in the Late Cretaceous and continued into the Miocene (Mattauer and Henry, 1974; Roure et al., 1989; Roest and Srivastava, 1991; Rosenbaum et al., 2002). The orogenic evolution began with the mid-Cretaceous hyper-extension of the Iberian margins, followed by the late Cretaceous subduction and collision with the European plate (Teixell et al., 2016). Foreland basins resulted on both sides of the fold and thrust belt (Puigdefbregas and Souquet, 1986; Muñoz, 1992; Gómez-Gras et al., 2016). The Southern Pyrenean foreland basin was active between the Late Cretaceous and the Oligocene, and contains well-preserved sedimentary archives of continental and marine environments.

The Tremp-Graus Basin is located in the South-Central Pyrenean Foreland Basin (Spain), delimited by the Boixols Thrust in the north and the Montsec Thrust to the south (**Fig. 1C**). During the Palaeocene, the Tremp-Graus Basin was dominated by continental sedimentation sourced from the Pyrenees (Gómez-Gras et al., 2016). The continental deposits of the Thanetian Espugafreda Formation (Fm.) predominantly represent floodplain sediment accumulation and consist of clay, silt, carbonate nodules, and Microcodium grains, with some isolated sandy to conglomeratic channels (Puigdefbregas and Souquet, 1986; Dreyer, 1993; Schmitz and Pujalte, 2003, 2007).

2.1. The Espugafreda section

The Espugafreda section (42°14'50" N; 0°45'13" E, **Fig. 1B**) has been widely studied for its well-preserved Palaeocene-Eocene sedimentary record (Schmitz and Pujalte, 2003; Baceta et al., 2005; Khozyem, 2013; Tremblin et al., 2022; Basilici et al., 2022; Jaimes-Gutierrez et al., 2024) (**Fig. 1D**). The Upper Thanetian sediments belong to the Espugafreda Fm. in the Tremp Group of the Tremp-Graus Basin (Dreyer, 1993). This formation consists of coarse-grained stream deposits intercalated with red floodplain sediments that are rich in carbonate nodules



and characterised by mature paleosols. The PETM sediments have been classified into five stratigraphic members (Pujalte and Schmitz, 2005; Pujalte et al., 2014; Colomera et al., 2017; Basilici et al., 2022). Member 1 belongs to the Esplugafreda Fm. and consists of a fining-upwards sequence of conglomerates and cross-laminated sandstones, known as the Incised Valley Fill (IVF) sediments. During this interval, a first negative carbon isotope excursion (CIE) marks the Pre-Onset Excursion (POE) (Khozyem, 2013; Tremblin et al., 2022; Jaimes-Gutierrez et al., 2024). Member 2 at the onset of the Ypresian is represented by the Claret Conglomerate (Pujalte and Schmitz, 2005), a 3-5 m thick conglomeratic unit, corresponding to a braid plain which has been interpreted as the proximal part of a megafan (Schmitz and Pujalte, 2007). Member 3, the Yellowish soils, consists of yellow mudstone with purple mottling, and the main body of the CIE is recorded during this interval (Pujalte and Schmitz, 2005). Member 4, consisting of red soil with gypsum, and Member 5, composed of light red mudstones with scarce carbonate nodules, correspond to the recovery interval of the PETM in this locality (Pujalte and Schmitz, 2005; Baceta et al., 2011; Khozyem, 2013; Pujalte et al., 2014; Tremblin et al., 2022; Basilici et al., 2022).

2.2. The Rin section

The Rin section (42°19'42.01"N; 0°32'42.16"E, **Fig. 1B and Fig. 4**) is a Palaeocene-Eocene sequence comprising mudstone-dominated alluvial deposits and very shallow marine carbonate alternations, indicating episodes of transgression and regression on the coastal plain (Schmitz and Pujalte, 2007) (**Fig. 1**). The upper Esplugafreda Fm. soils are characterised by grey mottling and sparse iron nodules, with preserved paedogenic features such as peds. Member 1, the IVF, consists of 4 m-thick reddish-yellow soils that are rich in carbonate nodules. Member 2, the Claret Conglomerate, outcrops as a 3 m-thick calcareous conglomerate with pale red clay pockets, and has sparse carbonate nodules and charophyte occurrences. Member 3, the Yellowish soils, consists of 13 m-thick reddish-yellow clays and silts. The base of Member 3 records sparse occurrences of lignite and carbonate nodules. Member 4 is not preserved in the Rin section, and the upper 3 m of the sequence consists of Member 5, which has light grey to reddish yellow soils with grey mottling, before the overlying Alveolina Limestone.

240

241



242

243

244

245

Figure 4. Rin section between the upper Thanetian and lower Ypresian. Members 1-5 described in the literature for the Esplugafreda section can be identified in the Rin section, except that Member 4 from the recovery phase of the PETM has not been preserved.

246

3. Material and methods

247

3.1. Size fraction separation

248

249

250

251

252

253

Standard protocols (e.g., Adatte et al., 1996; Bauer et al., 2016) were followed for decarbonation and size fraction separation at the Institute of Earth Sciences clay laboratory at the University of Lausanne (ISTE-UNIL). Samples (~5 g) were leached with 10% HCl for 30 min in a bubble bath, including 3 min in an ultrasonic bath, to disaggregate sediments and dissolve calcite. Distilled water was used to remove the acid until a neutral pH was obtained. Subsequently, the <2 µm fraction was separated by settling and enhanced with a centrifuge. Settling and extraction were repeated three times.

254

3.2. Clay mineralogy

255

256

257

258

259

The clay minerals were identified on air-dried and ethylene glycol-solvated samples at ISTE-UNIL following the protocol described in Adatte et al. (1996). An aliquot of the separated size fractions was pipetted on glass slides and dried at room temperature. The air-dried samples were further analysed with a Thermo Scientific ARL X'TRA powder diffractometer equipped with a Cu anode, operated at 45 kV and 40 mA. The step size was 0.02, with a scan rate of 0.5-1.2/min. Samples were glycolated to identify smectite (Moore and Reynolds, 1992).



260 Diffractograms were analysed using the XRDWin software, where the background was removed, and a
261 deconvolution was performed for overlapping peaks (e.g., K002 and Ch004).

262 3.3. Nodule Purification

263 Carbonate nodules were washed with running distilled water until visible clay clumps were removed. They were
264 then placed in a beaker with distilled water and in an ultrasonic bath to remove the remaining clay particles. A
265 second round in the ultrasonic bath was then carried out with some drops of HCl 10 M in order to remove the
266 outermost layer. The nodules were later washed in running distilled water, dried at 40 °C, and ground.

267 3.4. Rock-Eval Pyrolysis

268 Organic matter analyses were performed on powdered bulk rock samples using a Rock-Eval 6 at ISTE-UNIL,
269 following standard methodology (Espitalie et al., 1985; Behar et al., 2001). For calibration, the IFP 160000
270 standard was used. The Rock-Eval pyrolysis parameters measured were hydrogen index (HI, mg HC/g TOC, HC
271 = hydrocarbons), oxygen index (OI, mg CO₂/g TOC), Tmax (°C), and total organic carbon content (TOC, wt.%).
272 The HI, OI, and Tmax values give an overall measurement of the type and degree of maturation of the organic
273 matter (e.g., Espitalie et al., 1985).

274 3.5. Isotope geochemistry

275 3.5.1. Organic matter carbon isotopes

276 The carbon isotope composition of the decarbonated bulk rock samples was determined at the Institute of Earth
277 Surface Dynamics at the University of Lausanne (IDYST-UNIL) by elemental analysis/isotope ratio mass
278 spectrometry (EA/IRMS). The EA/IRMS system consisted of a Carlo Erba 1108 (Fisons Instruments, Milan, Italy)
279 elemental analyser connected to a Delta V Plus isotope ratio mass spectrometer via a ConFlo III split interface
280 (both Thermo Fisher Scientific, Bremen, Germany) operated under continuous helium (He) flow (Spangenberg,
281 2006; Spangenberg and Zufferey, 2019). The carbon isotope compositions were reported in the delta (δ) notation
282 as permil (‰) variations of the molar ratio of the heavy to light isotope (¹³C/¹²C) relative to the international
283 standard Vienna Pee Dee Belemnite limestone (VPDB). For calibration and normalisation of the measured δ¹³C
284 values to the international scales (VPDB-LSPVEC lithium carbonate scale), a 4-point calibration was used with
285 international reference material (RM) and in-house standards (Spangenberg and Zufferey, 2019). The used
286 standards included UNIL-Glycine (δ¹³C = -26.10 ± 0.05‰), UNIL-Urea-1 (δ¹³C = -43.00 ± 0.04‰), UNIL-
287 Pyridine (δ¹³C = -29.25 ± 0.06‰), and the RM USGS24 graphite (δ¹³C = -16.05 ± 0.04‰). Analyses were done
288 in duplicates. The accuracy of the analyses was checked periodically through the analysis of international RM
289 standards not used for calibration. The reproducibility and precision of the EA/IRMS δ¹³C analyses were
290 determined by the standard deviation of separately replicated analyses and were better than 0.1‰.

291 3.5.2. Lithium isotopes

292 Sample digestion, column chemistry, and mass spectrometry were conducted in the London Geochemistry and
293 Isotope Centre (LOGIC) laboratories at University College London (UCL) and Birkbeck, University of London.
294 Clay samples were subjected to bulk digestion using concentrated HF, HNO₃, and HClO₄ in Teflon beakers on a
295 hot plate at 130 °C, followed by steps in concentrated HNO₃ and 6 M HCl. The carbonate nodules were subject
296 to leaching to separate the carbonate and detrital fractions. The carbonate fraction was extracted by leaching ~100
297 mg of sample in 8 ml 0.1 M HCl for 1 h (Pogge von Strandmann et al., 2013; Wilson et al., 2021), allowing a
298 maximum of ~40 mg of calcium carbonate to be dissolved.

299
300 A standard method of elution was applied for lithium isotope separation in 0.2 M HCl. Two-column passes were
301 applied through AG50W-X12 resin to ensure matrix removal (Pogge von Strandmann et al., 2013). Given that
302 lithium isotopes are fractionated during ion chromatography, sample splits were collected before and after the
303 lithium collection interval to assess column yields. For example, a 1% loss in yield at UCL has been assessed to
304 lead to an offset of 1.7‰ (Wilson et al., 2021). Here, yields between two column passes were 99.8-100%,
305 indicating excellent recovery.

306
307 Lithium isotope measurements were performed on a Nu Plasma 3 MC-ICP-MS at UCL, using a Cetac Aridus 2
308 desolvation system, ‘super-lithium’ cones, and standard-sample bracketing with the IRMM-016 Li standard
309 (Pogge von Strandmann et al., 2019). Samples were measured at least three times within an analytical session,
310 with each measurement integrating ~50 s, and the reported values are the mean and standard deviation (2sd) of
311 these values, given in permil (‰) relative to the IRMM-016 standard. Accuracy and external reproducibility were



assessed using seawater and USGS standard BCR-2, which gave $\delta^7\text{Li}$ values of $+31.3 \pm 0.6\text{‰}$ (2sd, $n = 28$) and $+2.5 \pm 0.3\text{‰}$ ($n = 5$), respectively.

3.5.3. Neodymium isotopes and rare earth element concentrations

After decarbonisation using 10% HCl for 30 min, clays were separated from decarbonated sediments into $<0.5 \mu\text{m}$ and $0.5\text{--}2 \mu\text{m}$ (analytical protocol for size fraction separation reported in Jaimes-Gutierrez et al., 2024). A total of 18 samples (8 in the $<0.5 \mu\text{m}$ size fraction and 10 in the $0.5\text{--}2 \mu\text{m}$ size fraction) were analysed for their neodymium (Nd) isotopic composition and their Nd and samarium (Sm) concentrations. Aliquots of about 1.5 mg of each clay fraction followed a sequential leach procedure to remove Fe-Mn oxides and organic matter, based on the protocol of Bayon et al. (2002) and Gutjahr et al. (2007), slightly adapted. Fe-Mn oxides were removed using a solution of 0.5 M Hydroxylamine hydrochloride in 20% v/v for 48h. Then, the organic matter was removed with a 5% H_2O_2 solution during 48h.

The leached samples were dried and digested by alkaline fusion following the protocol of Bayon et al. (2009), along with certified standards (BHVO-2, BRC-2) from the United States Geological Survey (USGS). Approximately 50 mg of each sample underwent alkaline fusion in a carbon crucible with 0.6 g of NaOH and 1.2 g of Na_2O_2 heated at 650°C for 12 min in a furnace, before adding ultrapure water in which Fe-hydroxides precipitated, concentrating rare earth elements. After centrifugation, the samples were dissolved in 3 ml HCl 4 M.

From this solution, an aliquot of 0.3 ml was extracted for analyses of Nd and Sm concentrations. Part of the samples were measured for their Nd and Sm concentrations on an Agilent 7500 quadrupole ICP-MS spectrometer in the Laboratoire Magmas et Volcans (LMV) in Clermont-Ferrand (France) and quantified using standard bracketing with a solution of BHVO-2 during the session. Accuracy and reproducibility were assessed using two BHVO-2 and one BCR-2 samples among the samples. Deviations of Nd and Sm concentrations from these standards were below 11%. The other part of the samples were measured for their Nd and Sm concentrations on a Thermo Scientific X-Series II®, at the Pole Spectrométrie Océan in Brest (France) and quantified using multi-element calibration standards prepared from single element standards purchased from SCP science (Baie d'Urfé, Québec, Canada). Accuracy and reproducibility were assessed using one BHVO-2 and one BCR-2, which were analysed among the samples. Deviations of Nd and Sm concentrations from these standards were below 7 %.

Purified neodymium fractions were isolated from the mother solution by ion chromatography following the protocol described in Gaitan et al. (2023) for the low-pressure, automated column chromatography PrepFAST-MC® system device, using AG50W-X8 (200–400 mesh) resin for rare earth element separation and Ln Spec (50–100 μm) for Nd separation. Part of the neodymium isotopic measurements was performed on a MC-ICP-MS Neptune Plus (Thermo Scientific) at the Laboratoire Magmas et Volcans in Clermont-Ferrand (France). Ratios were corrected for mass bias using an exponential law and a $^{143}\text{Nd}/^{144}\text{Nd}$ ratio of 0.7219. Mass-bias-corrected $^{143}\text{Nd}/^{144}\text{Nd}$ were normalised to a JNdI-1 value of 0.512115 (Tanaka et al., 2000). Repeated measurements of JNdI-1 throughout the session gave an external reproducibility of ± 0.000009 (2σ , $n = 15$), corresponding to ± 0.18 in the standard $\varepsilon_{\text{Nd}}(0)$ notation. Analyses of two BHVO-2 reference materials yielded a $^{143}\text{Nd}/^{144}\text{Nd}$ ratio of 0.512991 ± 0.000005 for each, close to the published values of 0.512990 ± 0.000010 (Weis et al., 2005). The other part of the samples was analysed on an MC-ICP-MS Neptune Plus (Thermo Scientific) at the ENS of Lyon (France). Ratios were corrected for mass bias using an exponential law and a $^{143}\text{Nd}/^{144}\text{Nd}$ ratio of 0.7219. Mass-bias-corrected $^{143}\text{Nd}/^{144}\text{Nd}$ values were normalised to a JNdI-1 value of 0.512115 (Tanaka et al., 2000). Repeated measurements of JNdI-1 throughout the session gave an external reproducibility of ± 0.000018 (2σ , $n = 16$), corresponding to ± 0.34 in the standard $\varepsilon_{\text{Nd}}(0)$ notation. Analyses of four BHVO-2 reference materials gave an average $^{143}\text{Nd}/^{144}\text{Nd}$ ratio of 0.512985 ± 0.000009 for each, close to the published values of 0.512990 ± 0.000010 (Weis et al., 2006).

The data are reported in the standard epsilon notation $\varepsilon_{\text{Nd}} = [((^{143}\text{Nd}/^{144}\text{Nd})_{\text{sample}} / (^{143}\text{Nd}/^{144}\text{Nd})_{\text{CHUR}}) - 1] \times 10^4$, corrected for the radioactive decay of ^{147}Sm to ^{143}Nd based on the Nd and Sm concentrations measured for each sample ($^{147}\text{Sm}/^{144}\text{Nd} = \text{Sm}/\text{Nd} \times 0.6049$), an age of 55.8 Ma, and the ^{147}Sm radioactive decay constant λ ($6.54 \times 10^{-12} \text{ an}^{-1}$; Lugmair & Marti, 1977). The CHUR (CHondritic Uniform Reservoir) $^{143}\text{Nd}/^{144}\text{Nd}$ ratio was also corrected using a $^{147}\text{Sm}/^{144}\text{Nd}$ ratio of 0.1960 and a present-day value of 0.512630 (Bouvier et al., 2008).

4. Results

4.1. Clay mineralogy in the Rin section

The clay mineralogy in the Rin section (Fig. 5D, Table S1) comprises mixed-layer illite-smectite (I/S), with a mean abundance of 34 ± 11 (1 σ) wt.%; illite, 29 ± 9 wt.%; kaolinite, 30 ± 11 wt.%; and minor chlorite, 7 ± 5



wt.%. The pre-PETM samples have a mixed-layer I/S abundance of 42 ± 10 %, decreasing to 32 ± 10 wt.% during the body of the PETM. The kaolinite abundance increases from 22 ± 14 wt.% to 32 ± 9 wt.% during the PETM body, while the illite and chlorite abundances remain stable.

4.2. Organic matter carbon isotopes in the Rin section

Throughout the section, the mean $\delta^{13}\text{C}_{\text{OM}}$ value is -25.7 ‰, with a standard deviation (1σ) of 1.2 ‰ (Fig. 5A, Table S2). The pre-PETM samples, between 5.8 and 9.4 m, have a mean value of -23.5 ± 0.5 ‰. A negative excursion begins in samples at 10.7 and 11.4 m, with values decreasing to -24.6 ± 0.1 ‰. The most depleted values occur between 12.8 and 38.9 m, with a mean of -26.3 ± 0.5 ‰. The final sample at 39.5 m, below the Alveolina Limestone, suggests a return to pre-PETM levels, with a value of -23.7 ‰.

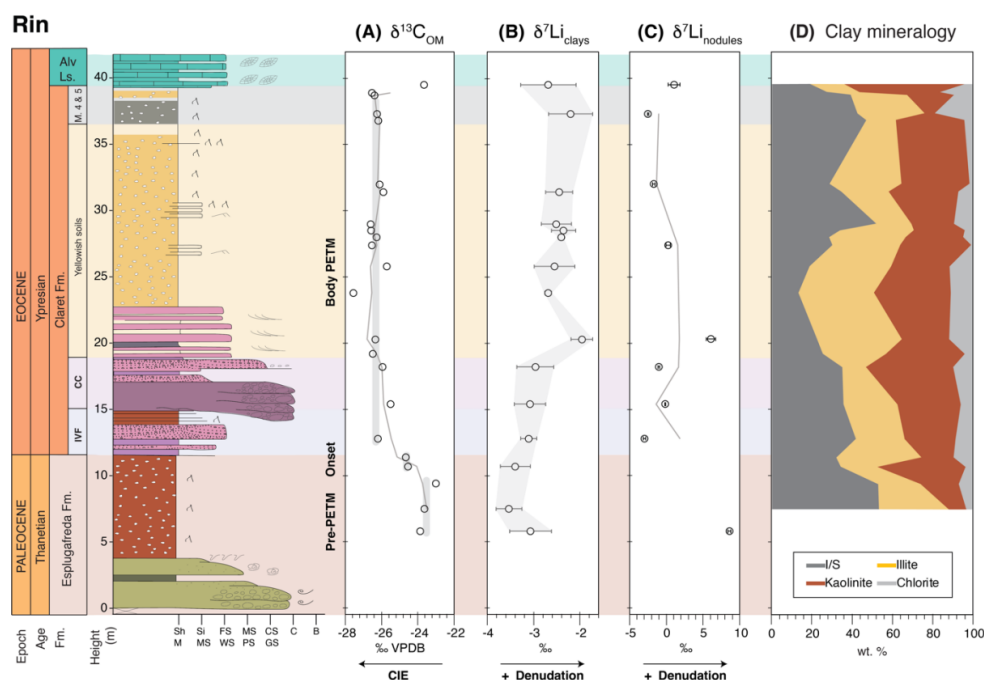


Figure 5. Rin section isotopes and clay mineralogy. (A) The $\delta^{13}\text{C}_{\text{OM}}$ record shows the negative Carbon Isotope Excursion (CIE), with an onset before the Claret Conglomerate and sustained negative values until the Alveolina Limestone. (B) The CIE was accompanied by a positive excursion in lithium isotopes of the clays ($\delta^7\text{Li}_{\text{clays}}$), reaching a 0.9 ‰ excursion in the Yellowish soils member. (C) Lithium isotopes in the carbonate nodules showed high variability and a less conclusive trend, suggesting clay contamination. (D) Rin section clay mineralogy. The pre-PETM and body intervals were determined based on the $\delta^{13}\text{C}_{\text{OM}}$ record and the stratigraphy. Grey bars in A represent average values for $\delta^{13}\text{C}_{\text{OM}}$ in the Pre-PETM and Syn-PETM intervals, and the analytical uncertainty of $\delta^7\text{Li}_{\text{clays}}$.

4.3. Lithium isotopes

The clays of the Rin section have a mean lithium isotope composition of -2.9 ± 0.5 ‰ (1σ) (Fig. 5B, Table S2). Between 5.8 and 18.2 m, the mean composition is -3.4 ± 0.2 ‰. Above this, from 20.3 to 39.5 m, the mean composition is -2.6 ± 0.2 ‰, which corresponds to a shift towards more positive values of ~ 0.8 ‰. The minimum value of -3.7 ‰ is seen before the Claret Conglomerate, and the maximum value of -2.2 ‰ occurs immediately after the Claret Conglomerate, indicating a total range of up to ~ 1.5 ‰. The $\delta^7\text{Li}$ values measured on carbonate nodules have a maximum value of 8.6 ‰, a minimum value of -3.0 ‰, and a mean composition of 0.9 ± 4.0 ‰ (Fig. 5C). No clear temporal trend is observed in the $\delta^7\text{Li}_{\text{nodules}}$ record.

At the Esplugafreda section, the clays have a mean lithium isotope composition of -3.7 ± 0.7 ‰ (Fig. 6B, Table S3). The pre-PETM samples (0-10 m and 21-28 m, Jaimes-Gutierrez et al., 2024 and references therein) have a



mean composition of $-3.8 \pm 0.2\text{‰}$. The POE samples ($\sim 15\text{--}21\text{ m}$) have a composition of $-3.2 \pm 0.2\text{‰}$, and the syn-PETM sediments have a composition of $-3.0 \pm 0.2\text{‰}$. The post-PETM sediments have a composition of $-4.5 \pm 0.4\text{‰}$.

4.4. Neodymium isotopes

The $0.5\text{--}2\text{ }\mu\text{m}$ clays throughout the Esplugafreda section have a mean $\epsilon_{\text{Nd}}(t = 55.8\text{ Ma})$ composition of -10.94 ± 0.16 (2σ), while the $<0.5\text{ }\mu\text{m}$ fraction had an average composition of -11.88 ± 0.11 (Fig. 6C, Table S4). In comparison, the typical analytical uncertainty on any individual sample measurement was 0.21 (2σ). Hence, these values are considered constant, with no deviation significantly outside the analytical uncertainty. Additional neodymium isotope measurements on the $<0.5\text{ }\mu\text{m}$ fraction are also indistinguishable from those on the $0.5\text{--}2\text{ }\mu\text{m}$ fraction (Fig. 6C).

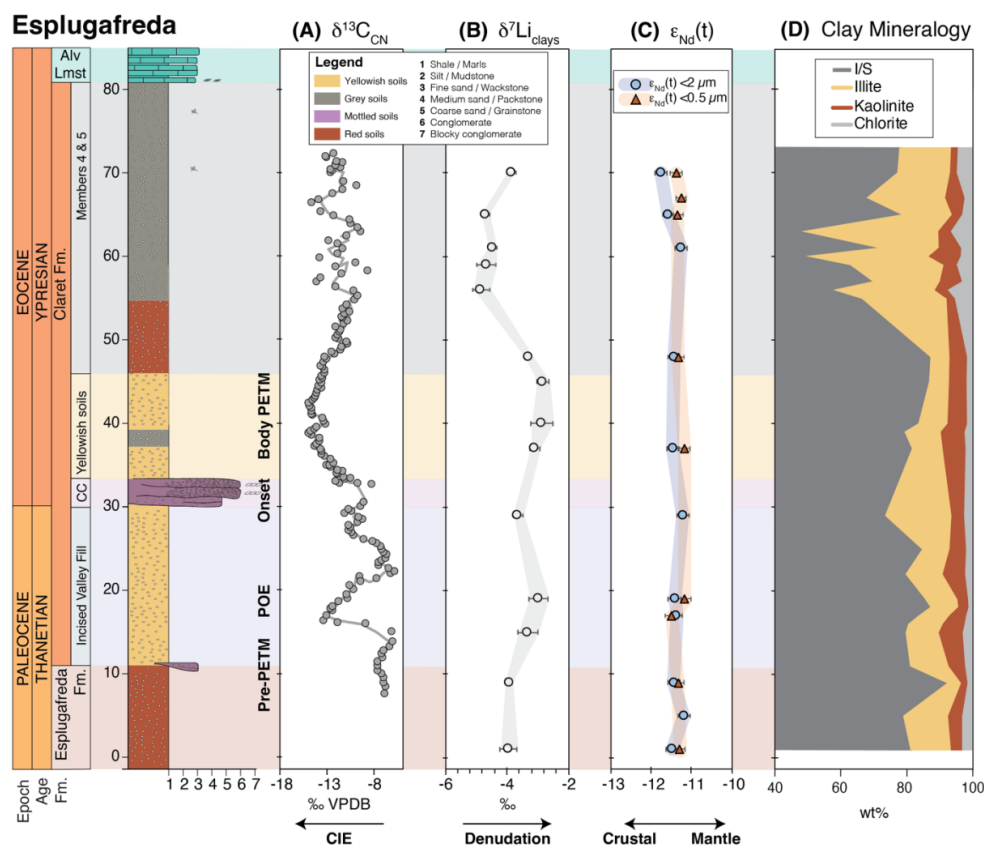


Figure 6. Esplugafreda section isotopes and clay mineralogy. (A) The $\delta^{13}\text{C}$ record from microcrystalline carbonate nodules (from Khozyem, 2013) shows a negative carbon isotope excursion during the Pre-Onset Excursion (POE) and the main body of the PETM. (B) There were positive excursions in lithium isotopes of the clays ($\delta^7\text{Li}_{\text{clays}}$) during both the POE and the main CIE of the PETM. (C) Neodymium isotopes ($\epsilon_{\text{Nd}}(t = 55.8\text{ Ma})$) show no variation throughout the section, indicating constant provenance. (D) Esplugafreda section clay mineralogy (modified from Jaimes-Gutierrez et al., 2024).

5. Discussion

5.1. The PETM in the Rin section

The PETM sediments in the Rin section represent an archive of the climatic perturbation in a coastal terrestrial setting (Pujalte et al., 2014; Prieur et al., 2025). This locality records a negative $\delta^{13}\text{C}_{\text{OM}}$ excursion of -2.8‰ from pre- to syn-PETM (Fig. 5), in agreement with the CIE excursion of $3\text{--}5\text{‰}$ identified in other southern Pyrenean sections and other global settings (e.g., Schmitz et al., 2001; Schmitz and Pujalte, 2007; McInerney and Wing,



2011; Pujalte et al., 2015). The slightly reduced magnitude compared to the global record is consistent with observed systematic differences in the CIE across different types of terrestrial archives, with paleosol carbonates typically recording a 1-2 ‰ larger CIE than paleosol organic matter (Bowen et al., 2004; Cotton et al., 2015; Gallagher et al., 2019). We do not identify the POE in the Rin section, and we suggest that it may have been missed due to its occurrence further down in the section. Likewise, the recovery to pre-PETM values is also largely absent, with just one sample below the Alevolina Limestone showing less depleted $\delta^{13}\text{C}_{\text{OM}}$ values.

The five members recognised in the Clare Fm., show an evolution from the eastern terrestrial setting into the western marine domain. At Esplugafreda, the five members are recorded (Basilici et al., 2022 and references therein), including Member 1, IVF (Pre-PETM); Member 2, the CC (Onset at Esplugafreda); Member 3, Yellowish soils (syn-PETM, or body of the PETM); Member 4, red paleosols with gypsum; and Member 5, consisting of red mudstones with carbonate nodules (e.g., Schmitz and Pujalte, 2007; Baceta et al., 2011; Pujalte et al., 2014; Colomera et al., 2017; Basilici et al., 2022). However, Member 4, the gypsum-rich member, only occurs in the eastern part of the basin (Pujalte et al., 2014). Given the coastal position of the Rin section, at the marine-continental transition and only ~20 km east of the Serraduy section, the westernmost expression of the interfingering between continental deposits from the Esplugafreda Fm. and marine carbonates (Prieur et al., 2025), the absence of Member 4 supports a further downstream position of the Rin section relative to the Esplugafreda floodplain section.

Duller et al. (2019) estimated a lag time of approximately 16.5 ± 7.5 kyr between the CIE and the onset of coarse-grained deposition at terrestrial sites in the Pyrenees. While sections such as Tendrui, Claret, and Campo (Pujalte et al., 2009; Domingo et al., 2009) display a stratigraphic offset consistent with this lag, the Esplugafreda section does not show such an offset (Duller et al., 2019). In the Rin section discussed here, we observe a clear offset between the onset of the CIE and the arrival of coarse-grained sediments, specifically the Claret Conglomerate (Fig. 5). To correctly position the lag time and explore the missing POE, future work could focus on high-resolution $\delta^{13}\text{C}$ characterisation of the section.

The clay mineralogy at Rin further suggests a potential signal propagation effect. A shift from smectite-dominated clays during the pre-PETM interval to an increase in kaolinite during the syn-PETM interval (Fig. 5D) could indicate a transition to more hydrolysing conditions and to an increase in weathering intensity, or enhanced erosion of former sedimentary formations rich in kaolinite. However, this trend also corresponds to a downstream transition from authigenic smectite-rich paleosols at Esplugafreda (Fig. 6D) (e.g., Khozyem, 2013; Basilici et al., 2022; Jaimes-Gutierrez et al., 2024) to kaolinite-dominated sediments in the Zumaia deep-marine section (Gawenda et al., 1999; Schmitz et al., 2001; Bolle and Adatte, 2001). This mineralogical gradient from Esplugafreda to Rin and Zumaia underscores the system connectivity across the basin (Pujalte et al., 2014). However, such variations in clay composition may also reflect differences in sediment provenance, although temporal changes are not observed in the ϵ_{Nd} record from Esplugafreda; differential mineral transport; enhanced floodplain weathering; increased proportion of eroded sedimentary formations downstream, bringing reworked kaolinite (Pujalte et al., 2015); or a larger catchment area feeding the marine system (Chamley, 1989 and references therein).

5.2. Evolution of weathering intensity in the continental realm of the Southern Pyrenees

Marine and terrestrial $\delta^7\text{Li}$ records in both detrital and carbonate archives consistently show a negative excursion from pre-PETM to syn-PETM sediments. Pogge von Strandmann et al. (2021) documented a negative $\delta^7\text{Li}$ excursion of ~3‰ during the PETM in several marine carbonate sections and in detrital shales, indicating intensified global erosion rates (by 2–3×) and a 50–60% increase in silicate weathering fluxes, which was proposed to have contributed to climate stabilisation. Ramos et al. (2022) also found a negative $\delta^7\text{Li}_{\text{clays}}$ excursion, albeit with a smaller magnitude of ~1.5‰, in fine sediments of the Bighorn Basin, North America during the PETM, and this change was sustained during the recovery phase. Consistent with these results, Chen et al. (2023) found a negative $\delta^7\text{Li}_{\text{clays}}$ excursion of ~3‰ in the Nanyang Basin, which, together with the negative $\delta^7\text{Li}$ excursion in carbonates, was interpreted as recording a doubling of the regional silicate weathering intensity during the PETM.

In contrast, our $\delta^7\text{Li}_{\text{clays}}$ records from Rin and Esplugafreda both show a positive (~1‰) lithium isotope excursion in the continental Southern Pyrenees during the onset and body of the PETM. The $\delta^7\text{Li}$ values from carbonate nodules at Rin show greater variability (Fig. 5C), but remain inconclusive due to the potential clay contamination or cation exchange between clays and carbonates (e.g., Pogge Von Strandmann et al., 2019). Given the high Li content in silicate minerals, even a minor clay particle content in the nodules could contaminate the signature. Critically, the invariant ϵ_{Nd} composition of the samples in both size fractions throughout the Esplugafreda record

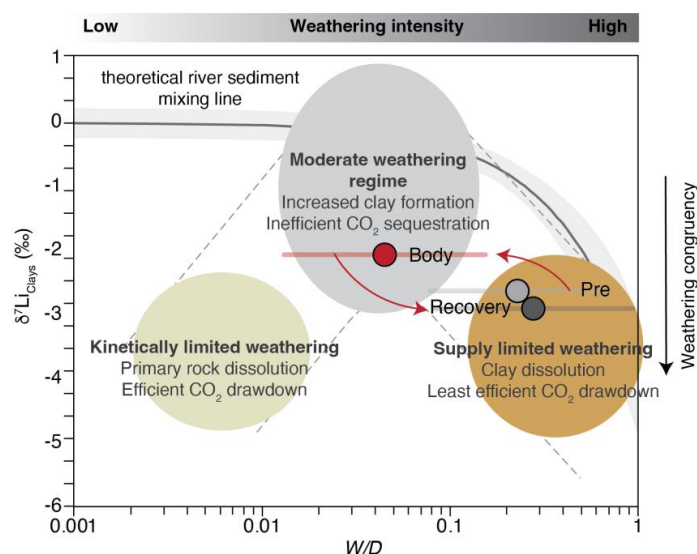


481 supports a constant provenance of the sediments, which suggests that the $\delta^7\text{Li}_{\text{clays}}$ records can be reliably
482 interpreted as a reflection of weathering regime changes in response to the climatic perturbation.

483
484 We interpret the positive $\delta^7\text{Li}_{\text{clays}}$ excursion during the PETM as a shift towards increased incongruent weathering,
485 characterised by enhanced clay formation in the floodplain deposits. This regime would be characterised by
486 increased chemical weathering, but relatively greater increases in physical erosion and sediment transport (e.g.,
487 Pujalte et al., 2015; Chen et al., 2018; Prieur et al., 2024), due to enhanced runoff causing short water residence
488 times and rapid sediment export (i.e., lower W/D; Fig. 7). Hydrological changes during the PETM are widely
489 documented in the Southern Pyrenees (Schmitz and Pujalte, 2007; Pujalte et al., 2015; Chen et al., 2018; Rush et
490 al., 2021; Prieur et al., 2024, 2025; Jaimes-Gutierrez et al., 2024) and likely played a central role in driving those
491 weathering changes. A shift towards more intense, episodic rainfall, without an increase in mean annual
492 precipitation (Rush et al., 2021), could have reduced infiltration, increased runoff, and shortened water–mineral
493 interaction times. These processes would lead to decreased clay formation in the uplands (Kump et al., 2000;
494 Riebe et al., 2004), but increased clay production and accumulation in lowlands, where longer sediment residence
495 times promote authigenic clay formation.

496
497 Increasing evaporation, as recorded by gypsum lenses in Esplugafreda (Baceta et al., 2011; Khozyem, 2013;
498 Jaimes-Gutierrez et al., 2024 and references therein), could also result in oversaturated waters, which would favour
499 clay formation, with higher clay $\delta^7\text{Li}$ compositions reflecting equilibrium with the water composition (Pogge von
500 Strandmann et al., 2023). With an increase in clay formation in the floodplains, the isotopically heavier river
501 waters would generate isotopically heavier clays further downstream (Pogge von Strandmann et al., 2023).
502 Hydrological controls would also potentially enhance a positive $\delta^7\text{Li}_{\text{clays}}$ excursion with a weathering starting
503 point in a supply-limited weathering domain (Fig. 7), as faster runoff would result in less time for water–rock
504 interaction, leading to less time for clay formation (Zhang et al., 2022). Overall, rapid sediment transport and short
505 sediment residence times would be decisive in limiting the degree of weathering, despite an increase in clay
506 formation in the floodplains.

507



508

509 **Figure 7.** Weathering regime change from pre-PETM to syn-PETM based on $\delta^7\text{Li}_{\text{clays}}$ in the continental deposits
510 of the Southern Pyrenees. The floodplain records were characterised by a decrease in weathering intensity and
511 an increase in clay formation. Enhanced transport efficiency resulted in a major increase in physical erosion,
512 with reaction kinetics limiting chemical weathering. Modified from Dellinger et al. (2015, 2017). At low W/D, the
513 theoretical river sediment mixing line includes the effects of mixing with primary minerals.

514 Temperature effects on lithium isotope fractionation are minor in the Southern Pyrenees. While lithium isotope
515 fractionation during clay formation is temperature-dependent (Vigier et al., 2008; Li and West, 2014), the
516 fractionation factor (α) for incorporation in smectite is nearly constant across typical surface weathering
517 temperatures (Vigier et al., 2008). Considering the mean annual air temperatures for the continental Pyrenees were
518 a minimum of 23 °C pre-PETM and a maximum of 28 °C syn-PETM (Jaimes-Gutierrez et al., 2024), the resulting



maximum fractionation from pre-PETM to syn-PETM was -0.70‰ (Li and West, 2014). Although this fractionation towards more negative values may have had a small effect in reducing the magnitude of the excursion, it is evidently unable to account for the positive $\delta^7\text{Li}_{\text{clays}}$ shifts observed in the records. Hence, climatic and hydrological processes, rather than direct temperature effects, must dominate the $\delta^7\text{Li}$ signal.

The differences in $\delta^7\text{Li}$ values between river water and bedrock are controlled by the balance between lithium release by mineral dissolution and lithium removal by secondary mineral formation (Bouchez et al., 2013). The Southern Pyrenees during the PETM was a relatively high-erosion regime, such that physical erosion dominated, increasing the sediment supply and exposing fresh minerals. When erosion exposes fresh minerals, weathering rates increase with total denudation, albeit less strongly than the increases in erosion, consistent with shared controls on chemical weathering and physical denudation rates (Riebe et al., 2004). Even though high-relief regions produce weakly weathered sediments, their high sediment yields and moderate clay formation rates result in elevated weathering fluxes (Gaillardet et al., 1999). Therefore, we propose that the Southern Pyrenean floodplains record a shift from a high-weathering intensity regime to a moderate-weathering intensity regime during the PETM (Fig. 7). The pre-PETM conditions were characterised by a low reactivity of the parent lithology (Kump and Arthur, 1997; Caves Rugenstein et al., 2019), associated with the carbonate-rich, reworked sediments in the floodplain deposits, and hence low total weathering fluxes. The above scenario is also consistent with the "system-clearing" event documented in western North America (Foreman et al., 2012), where sediment transport surged in response to rapid climatic forcing, as well as with other Eocene warming events such as the Mid-Eocene Climatic Optimum, which saw a shift towards enhanced clay formation and a lower weathering intensity (Krause et al., 2023).

A possible explanation for the progressive increase in kaolinite content from Esplugafreda to Rin may reflect an evolving weathering signal during sediment transport from the hinterland towards the coastal plains, which potentially extended into the marine realm. This scenario supports a basin-wide connectivity between climate-driven terrestrial processes and marine sedimentary records. In addition, the increase in kaolinite content from Esplugafreda to Rin supports a shift in clay formation processes during the PETM. Kaolinite is typically associated with intense leaching and more advanced weathering, often forming under warm, humid, and periodically saturated conditions (Chamley, 1989; Velde and Meunier, 2008). Hence, its enrichment suggests either intensified in-situ clay formation in the floodplains or increased transport of weathered material from the uplands to the lowlands. In either case, this shift implies greater clay mineral production, consistent with a more incongruent weathering regime driving the observed positive $\delta^7\text{Li}_{\text{clays}}$ excursion. Alternatively, enhanced kaolinite supply from the erosion-driven exhumation of older sediments cannot be ruled out based on the current evidence.

Despite these insights, key questions remain unresolved. In particular, a comprehensive study of the provenance and evolution of clay mineralogy is still needed to determine to what extent the observed patterns along the sediment routing system reflect changes in weathering intensity, differential mineral transport, or sediment reworking. Equally important is the need to constrain the precise age of the clay formation in relation to the timing of the different phases of the PETM, which is critical for reconstructing the temporal dynamics of the weathering regime in the Southern Pyrenees. Addressing these gaps will be crucial for better understanding how continental weathering systems responded to extreme climatic perturbations in the past and how they may behave under future global warming scenarios.

6. Conclusions

We explored the silicate weathering response to the PETM in two terrestrial sections from the Tremp-Graus Basin of the Southern Pyrenees. These floodplain records show a positive $\delta^7\text{Li}_{\text{clays}}$ excursion, contrasting with the commonly observed global negative $\delta^7\text{Li}$ excursion in clays and carbonates. We interpret this excursion as reflecting a shift towards a moderate-intensity, incongruent weathering regime from initial high-intensity, supply-limited conditions. The high erosion rates associated with increased extreme rainfall events and channel mobility may have been the central factor influencing sediment residence times, with rapid sediment transport limiting the extent of chemical weathering. Nevertheless, the elevated denudation rates would have led to higher sediment and dissolved cation fluxes to the ocean, thereby enhancing regional CO_2 drawdown.

We explored two potential archives for recording continental weathering processes using lithium isotopes. The clay records show a distinct response, reflected in positive $\delta^7\text{Li}_{\text{clays}}$ excursions synchronous with the negative CIE. However, the $\delta^7\text{Li}_{\text{nODULES}}$ signal recorded in the carbonate nodules is less conclusive, and we interpret the strong temporal variability as a sign of potential contamination by clays in the nodules. Given that Li concentrations in silicate minerals are higher than carbonates by several orders of magnitude, even minor amounts of clays could



have resulted in a mixed response in the nodules. Future studies should explore weaker leaching approaches on such nodules and seek to validate such data with major and trace element analyses.

Provided coeval formation, the increase in kaolinite content from Esplugafreda to Rin provides mineralogical support for more hydrolysing conditions and clay formation during the PETM in the Tremp-Graus Basin, reinforcing the interpretation of more incongruent weathering under altered hydroclimatic conditions. Notably, the parent material in these floodplain paleosols is carbonate-rich and relatively unreactive. These results highlight the critical role of hydrological controls, especially rainfall intensity, runoff dynamics, and sediment residence time, in shaping continental weathering responses during extreme climate events.

Finally, we propose that to fully quantify weathering dynamics during the PETM in the Southern Pyrenees, further work is needed to: (1) constrain the chronology of clay formation; (2) trace the evolution of clay mineralogy and provenance from source to sink; and (3) integrate continental and marine weathering records across the sediment routing system. Together, these steps will be essential for refining our understanding of weathering behaviour and the associated climate feedbacks under rapid climatic perturbations, and for improving predictions of Earth's surface processes in semi-arid floodplain systems in future global warming scenarios.

Acknowledgments

We acknowledge funding from the European Union's Horizon 2020 research and innovation programme under the Marie Skłodowska-Curie grant agreement No. 860383 S2S FUTURE. D.J.W. was supported by a NERC independent research fellowship (NE/T011440/1). We thank Justine Blondet for her support in neodymium isotope chromatography.

Author contributions

R.J.G. performed sample collection, analytical work (clay mineralogy, RockEval, lithium and neodymium ion-exchange chromatography), data interpretation, visualisation, and manuscript writing.

M.P. contributed to sample collection, data interpretation, visualisation, and manuscript writing.

D.J.W. and P.A.E.P.V.S. contributed to analytical work on lithium isotopes, data interpretation, and manuscript writing.

E.P. conducted analytical work on neodymium isotopes, data interpretation, manuscript writing, and provided supervision.

T.A. conducted RockEval analyses, contributed to data interpretation, and provided supervision.

J.E.S. conducted $\delta^{13}\text{C}$ analyses on organic matter and contributed to data interpretation and manuscript writing.

S.C. acquired funding for the project, contributed to sample collection and data interpretation, and provided supervision.

Conflict of interest

The authors declare that they have no conflict of interest relevant to this study.

References

Adatte, T., Stinnesbeck, W., and Keller, G., 1996, Lithostratigraphic and mineralogic correlations of near K/T boundary clastic sediments in northeastern Mexico: Implications for origin and nature of deposition, *in* The Cretaceous-Tertiary Event and Other Catastrophes in Earth History, Geological Society of America, doi:10.1130/0-8137-2307-8.211.

Anderson, S.P., Von Blanckenburg, F., and White, A.F., 2007, Physical and Chemical Controls on the Critical Zone: Elements, v. 3, p. 315–319, doi:10.2113/gselements.3.5.315.

Baceta, J.I., Pujalte, V., and Bernaola, G., 2005, Paleocene corallgal reefs of the western Pyrenean basin, northern Spain: New evidence supporting an earliest Paleogene recovery of reefal ecosystems: Palaeogeography, Palaeoclimatology, Palaeoecology, v. 224, p. 117–143, doi:10.1016/j.palaeo.2005.03.033.

Baceta, J.I., Pujalte, V., Wright, V.P., and Schmitz, B., 2011, Carbonate platform models, sea/level changes and extreme climatic events during the Paleocene/ Eocene greenhouse interval: A basin-platform-coastal plain transect across the southern Pyrenean basin: 28th IAS Meeting of Sedimentology.



- 630 Barefoot, E.A., Nittrouer, J.A., Foreman, B.Z., Hajek, E.A., Dickens, G.R., Baisden, T., and Toms, L., 2022,
631 Evidence for enhanced fluvial channel mobility and fine sediment export due to precipitation
632 seasonality during the Paleocene-Eocene thermal maximum: v. 50, p. 116–120, doi:10.1130/G49149.1.
- 633 Basilici, G., Colombero, L., Soares, M.V.T., Arévalo, O.J., Mountney, N.P., Lorenzoni, P., de Souza Filho,
634 C.R., Mesquita, Á.F., and Janočko, J., 2022, Variations from dry to aquic conditions in Vertisols
635 (Esplugafreda Formation, Eastern Pyrenees, Spain): Implications for late Paleocene climate change:
636 Palaeogeography, Palaeoclimatology, Palaeoecology, v. 595, p. 110972,
637 doi:10.1016/j.palaeo.2022.110972.
- 638 Bauer, K.K., Vennemann, T.W., and Gilg, H.A., 2016, Stable isotope composition of bentonites from the Swiss
639 and Bavarian Freshwater Molasse as a proxy for paleoprecipitation: Palaeogeography,
640 Palaeoclimatology, Palaeoecology, v. 455, p. 53–64, doi:10.1016/j.palaeo.2016.02.002.
- 641 Bayon, G., Burton, K.W., Soulet, G., Vigier, N., Dennielou, B., Etoubleau, J., Ponzevera, E., German, C.R., and
642 Nesbitt, R.W., 2009, Hf and Nd isotopes in marine sediments: Constraints on global silicate
643 weathering: Earth and Planetary Science Letters, v. 277, p. 318–326, doi:10.1016/j.epsl.2008.10.028.
- 644 Bayon, G., German, C.R., Boella, R.M., Milton, J.A., Taylor, R.N., and Nesbitt, R.W., 2002, An improved
645 method for extracting marine sediment fractions and its application to Sr and Nd isotopic analysis:
646 Chemical Geology, v. 187, p. 179–199, doi:10.1016/S0009-2541(01)00416-8.
- 647 Behar, F., Beaumont, V., and De B. Pentead, H.L., 2001, Rock-Eval 6 Technology: Performances and
648 Developments: Oil & Gas Science and Technology, v. 56, p. 111–134, doi:10.2516/ogst:2001013.
- 649 Bolle, M.-P., and Adatte, T., 2001, Palaeocene- early Eocene climatic evolution in the Tethyan realm: clay
650 mineral evidence: Clay Minerals, v. 36, p. 249–261, doi:10.1180/000985501750177979.
- 651 Bouchez, J., Von Blanckenburg, F., and Schuessler, J.A., 2013, Modeling novel stable isotope ratios in the
652 weathering zone: American Journal of Science, v. 313, p. 267–308, doi:10.2475/04.2013.01.
- 653 Bouvier, A., Vervoort, J.D., and Patchett, P.J., 2008, The Lu–Hf and Sm–Nd isotopic composition of CHUR:
654 Constraints from unequilibrated chondrites and implications for the bulk composition of terrestrial
655 planets: Earth and Planetary Science Letters, v. 273, p. 48–57, doi:10.1016/j.epsl.2008.06.010.
- 656 Bowen, G.J., Beerling, D.J., Koch, P.L., Zachos, J.C., and Quattlebaum, T., 2004, A humid climate state during
657 the Palaeocene/Eocene thermal maximum: Nature, v. 432, p. 495–499, doi:10.1038/nature03115.
- 658 Bufer, A., Hovius, N., Emberson, R., Rugenstein, J.K.C., Galy, A., Hassenruck-Gudipati, H.J., and Chang, J.-M.,
659 2021, Co-variation of silicate, carbonate and sulfide weathering drives CO₂ release with erosion:
660 Nature Geoscience, v. 14, p. 211–216, doi:10.1038/s41561-021-00714-3.
- 661 Bufer, A., Rugenstein, J.K.C., and Hovius, N., 2024, CO₂ drawdown from weathering is maximized at moderate
662 erosion rates: Science, v. 383, p. 1075–1080, doi:10.1126/science.adk0957.
- 663 Carmichael, M.J. et al., 2017, Hydrological and associated biogeochemical consequences of rapid global
664 warming during the Paleocene-Eocene Thermal Maximum: Global and Planetary Change, v. 157, p.
665 114–138, doi:10.1016/j.gloplacha.2017.07.014.
- 666 Caves, J.K., Jost, A.B., Lau, K.V., and Maher, K., 2016, Cenozoic carbon cycle imbalances and a variable
667 weathering feedback: Earth and Planetary Science Letters, v. 450, p. 152–163,
668 doi:10.1016/j.epsl.2016.06.035.
- 669 Caves Rugenstein, J.K., Ibarra, D.E., and von Blanckenburg, F., 2019, Neogene cooling driven by land surface
670 reactivity rather than increased weathering fluxes: Nature, v. 571, p. 99–102, doi:10.1038/s41586-019-
671 1332-y.
- 672 Chamley, H., 1989, Clay Sedimentology: Berlin, Heidelberg, Springer Berlin Heidelberg, doi:10.1007/978-3-
673 642-85916-8.



- 674 Chen, Z., Ding, Z., Yang, S., Sun, J., Zhu, M., Xiao, Y., Tong, F., and Liang, Y., 2023, Strong Coupling
675 Between Carbon Cycle, Climate, and Weathering During the Paleocene-Eocene Thermal Maximum:
676 Geophysical Research Letters, v. 50, p. e2023GL102897, doi:10.1029/2023GL102897.
- 677 Chen, C., Guerit, L., Foreman, B.Z., Hassenruck-Gudipati, H.J., Adatte, T., Honegger, L., Perret, M., Sluijs, A.,
678 and Castellort, S., 2018, Estimating regional flood discharge during Palaeocene-Eocene global
679 warming: Scientific Reports, v. 8, p. 13391, doi:10.1038/s41598-018-31076-3.
- 680 Colomera, L., Arévalo, O.J., and Mountney, N.P., 2017, Fluvial-system response to climate change: The
681 Paleocene-Eocene Tremp Group, Pyrenees, Spain: Global and Planetary Change, v. 157, p. 1–17,
682 doi:10.1016/j.gloplacha.2017.08.011.
- 683 Cotton, J.M., Sheldon, N.D., Hren, M.T., and Gallagher, T.M., 2015, Positive feedback drives carbon release
684 from soils to atmosphere during Paleocene/Eocene warming: American Journal of Science, v. 315, p.
685 337–361, doi:10.2475/04.2015.03.
- 686 Dellinger, M., Bouchez, J., Gaillardet, J., Faure, L., and Moureau, J., 2017, Tracing weathering regimes using
687 the lithium isotope composition of detrital sediments: Geology, v. 45, p. 411–414,
688 doi:10.1130/G38671.1.
- 689 Dellinger, M., Gaillardet, J., Bouchez, J., Calmels, D., Louvat, P., Dosseto, A., Gorge, C., Alanoca, L., and
690 Maurice, L., 2015, Riverine Li isotope fractionation in the Amazon River basin controlled by the
691 weathering regimes: Geochimica et Cosmochimica Acta, v. 164, p. 71–93,
692 doi:10.1016/j.gca.2015.04.042.
- 693 Dessert, C., Dupré, B., Gaillardet, J., François, L.M., and Allège, C.J., 2003, Basalt weathering laws and the
694 impact of basalt weathering on the global carbon cycle: Chemical Geology, v. 202, p. 257–273,
695 doi:10.1016/j.chemgeo.2002.10.001.
- 696 Dickens, G.R., O'Neil, J.R., Rea, D.K., and Owen, R.M., 1995, Dissociation of oceanic methane hydrate as a
697 cause of the carbon isotope excursion at the end of the Paleocene: Paleocyanography, v. 10, p. 965–
698 971, doi:10.1029/95PA02087.
- 699 Dixon, J.L., and Von Blanckenburg, F., 2012, Soils as pacemakers and limiters of global silicate weathering:
700 Comptes Rendus. Géoscience, v. 344, p. 597–609, doi:10.1016/j.crte.2012.10.012.
- 701 Domingo, L., López-Martínez, N., Leng, M.J., and Grimes, S.T., 2009, The Paleocene–Eocene Thermal
702 Maximum record in the organic matter of the Claret and Tendry continental sections (South-central
703 Pyrenees, Lleida, Spain): Earth and Planetary Science Letters, v. 281, p. 226–237,
704 doi:10.1016/j.epsl.2009.02.025.
- 705 Dreyer, T., 1993, Quantified Fluvial Architecture in Ephemeral Stream Deposits of the Esplugafreda Formation
706 (Palaeocene), Tremp-Graus Basin, Northern Spain, in Marzo, M. and Puigdefàbregas, C. eds., Alluvial
707 Sedimentation, Wiley, p. 337–362, doi:10.1002/9781444303995.ch23.
- 708 Duller, R.A., Armitage, J.J., Manners, H.R., Grimes, S., and Jones, T.D., 2019, Delayed sedimentary response
709 to abrupt climate change at the Paleocene-Eocene boundary, northern Spain: Geology, v. 47, p. 159–
710 162, doi:10.1130/G45631.1.
- 711 Eichenseer, H., 1988, Facies Geology Of Late Maestrichtian To Early Eocene Coastal And Shallow Marine
712 Sediments (Tremp-Graus Basin, Northeastern Spain):
- 713 Eichenseer, H., and Luterbacher, H., 1992, The marine paleogene of the tremp region (NE Spain)-depositional
714 sequences, facies history, biostratigraphy and controlling factors: Facies, v. 27, p. 119–151,
715 doi:10.1007/BF02536808.
- 716 Espitalie, J., Deroo, G., and Marquis, F., 1985, La pyrolyse Rock-Eval et ses applications. Deuxième partie.:
717 Revue de l'Institut Français du Pétrole, v. 40, p. 755–784, doi:10.2516/ogst:1985045.



- 718 Foreman, B.Z., Heller, P.L., and Clementz, M.T., 2012, Fluvial response to abrupt global warming at the
719 Palaeocene/Eocene boundary: *Nature*, v. 491, p. 92–95, doi:10.1038/nature11513.
- 720 Gabet, E.J., and Mudd, S.M., 2009, A theoretical model coupling chemical weathering rates with denudation
721 rates: *Geology*, v. 37, p. 151–154, doi:10.1130/G25270A.1.
- 722 Gaillardet, J., Dupré, B., and Allègre, C.J., 1999, Geochemistry of large river suspended sediments: silicate
723 weathering or recycling tracer? *Geochimica et Cosmochimica Acta*, v. 63, p. 4037–4051,
724 doi:10.1016/S0016-7037(99)00307-5.
- 725 Gaitan, C.E., Pucéat, E., Pellenard, P., Blondet, J., Bayon, G., Adatte, T., Israel, C., Robin, C., and Guillocheau,
726 F., 2023, Late Cretaceous erosion and chemical weathering record in the offshore Cape Basin: Source-
727 to-sink system from Hf Nd isotopes and clay mineralogy: *Marine Geology*, v. 466, p. 107187,
728 doi:10.1016/j.margeo.2023.107187.
- 729 Gallagher, T.M., Cacciatore, C.G., and Breecker, D.O., 2019, Interpreting the Difference in Magnitudes of
730 PETM Carbon Isotope Excursions in Paleosol Carbonate and Organic Matter: Oxidation of Methane in
731 Soils Versus Elevated Soil Respiration Rates: *Paleoceanography and Paleoclimatology*, v. 34, p. 2113–
732 2128, doi:10.1029/2019PA003596.
- 733 Gawenda, P., Winkler, W., Schmitz, B., and Adatte, T., 1999, Climate and bioproductivity control on carbonate
734 turbidite sedimentation (Paleocene to earliest Eocene, Gulf of Biscay, Zumaia, Spain): *Journal of*
735 *Sedimentary Research*, v. 69, p. 1253–1261, doi:10.2110/jsr.69.1253.
- 736 Goddérès, Y., Donnadieu, Y., Tombozafy, M., and Dessert, C., 2008, Shield effect on continental weathering:
737 Implication for climatic evolution of the Earth at the geological timescale: *Geoderma*, v. 145, p. 439–
738 448, doi:10.1016/j.geoderma.2008.01.020.
- 739 Gómez-Gras, D., Roigé, M., Fondevilla, V., Oms, O., Boya, S., and Remacha, E., 2016, Provenance constraints
740 on the Tremp Formation paleogeography (southern Pyrenees): Ebro Massif VS Pyrenees sources:
741 *Cretaceous Research*, v. 57, p. 414–427, doi:10.1016/j.cretres.2015.09.010.
- 742 Gutjahr, M., Frank, M., Stirling, C.H., Klemm, V., Van De Flierdt, T., and Halliday, A.N., 2007, Reliable
743 extraction of a deepwater trace metal isotope signal from Fe–Mn oxyhydroxide coatings of marine
744 sediments: *Chemical Geology*, v. 242, p. 351–370, doi:10.1016/j.chemgeo.2007.03.021.
- 745 Hessler, A.M., Zhang, J., Covault, J., and Ambrose, W., 2017, Continental weathering coupled to Paleogene
746 climate changes in North America: *Geology*, v. 45, p. 911–914, doi:10.1130/G39245.1.
- 747 Hilton, R.G., 2023, Earth’s persistent thermostat: *Science*, v. 379, p. 329–330, doi:10.1126/science.adf3379.
- 748 Jaimes-Gutierrez, R., Adatte, T., Pucéat, E., Vennemann, T., Prieur, M., Wild, A.L., Khozyem, H., Vaucher, R.,
749 and Castellort, S., 2024, Deciphering Paleocene-Eocene Thermal Maximum Climatic Dynamics:
750 Insights From Oxygen and Hydrogen Isotopes in Clay Minerals of Paleosols From the Southern
751 Pyrenees: *Paleoceanography and Paleoclimatology*, v. 39, p. e2024PA004858,
752 doi:10.1029/2024PA004858.
- 753 Jones, M.T. et al., 2023, Tracing North Atlantic volcanism and seaway connectivity across the Paleocene–
754 Eocene Thermal Maximum (PETM): *Climate of the Past*, v. 19, p. 1623–1652, doi:10.5194/cp-19-
755 1623-2023.
- 756 Kennett, J.P., and Stott, L.D., 1991, Abrupt deep-sea warming, palaeoceanographic changes and benthic
757 extinctions at the end of the Palaeocene: *Nature*, v. 353, p. 225–229, doi:10.1038/353225a0.
- 758 Khozyem, H.M.A., 2013, Sedimentology, geochemistry and mineralogy of the Paleocene Eocene Thermal
759 Maximum (PETM): Sediment records from Egypt, India and Spain [Doctoral Dissertation]: Université
760 de Lausanne, 195 p.
- 761 Kısakürek, B., James, R.H., and Harris, N.B.W., 2005, Li and $\delta^7\text{Li}$ in Himalayan rivers: Proxies for silicate
762 weathering? *Earth and Planetary Science Letters*, v. 237, p. 387–401, doi:10.1016/j.epsl.2005.07.019.



- 763 Krause, A.J., Sluijs, A., Van Der Ploeg, R., Lenton, T.M., and Pogge Von Strandmann, P.A.E., 2023, Enhanced
764 clay formation key in sustaining the Middle Eocene Climatic Optimum: *Nature Geoscience*, v. 16, p.
765 730–738, doi:10.1038/s41561-023-01234-y.
- 766 Kump, L.R., and Arthur, M.A., 1997, Global Chemical Erosion during the Cenozoic: Weatherability Balances
767 the Budgets, *in* Ruddiman, W.F. ed., *Tectonic Uplift and Climate Change*, Boston, MA, Springer US,
768 p. 399–426, doi:10.1007/978-1-4615-5935-1_18.
- 769 Kump, L.R., Brantley, S.L., and Arthur, M.A., 2000, Chemical Weathering, Atmospheric CO₂, and Climate:
770 *Annual Review of Earth and Planetary Sciences*, v. 28, p. 611–667,
771 doi:10.1146/annurev.earth.28.1.611.
- 772 Li, G., and West, A.J., 2014, Evolution of Cenozoic seawater lithium isotopes: Coupling of global denudation
773 regime and shifting seawater sinks: *Earth and Planetary Science Letters*, v. 401, p. 284–293,
774 doi:10.1016/j.epsl.2014.06.011.
- 775 Maher, K., and Von Blanckenburg, F., 2023, The circular nutrient economy of terrestrial ecosystems and the
776 consequences for rock weathering: *Frontiers in Environmental Science*, v. 10, p. 1066959,
777 doi:10.3389/fenvs.2022.1066959.
- 778 Mattauer, M., and Henry, J., 1974, Pyrenees: *Special Publications*, v. 4, no.1, p. 3–21.
- 779 McInerney, F.A., and Wing, S.L., 2011, The Paleocene-Eocene Thermal Maximum: A Perturbation of Carbon
780 Cycle, Climate, and Biosphere with Implications for the Future: *Annual Review of Earth and Planetary*
781 *Sciences*, v. 39, p. 489–516, doi:10.1146/annurev-earth-040610-133431.
- 782 Misra, S., and Froelich, P.N., 2012, Lithium Isotope History of Cenozoic Seawater: Changes in Silicate
783 Weathering and Reverse Weathering: *Science*, v. 335, p. 818–823, doi:10.1126/science.1214697.
- 784 Moore, D.M., and Reynolds, R.C., 1992, *Moore, Reynolds 1997_X-Ray Diffraction.pdf*: New York, Oxford
785 University Press, 401 p.
- 786 Moulton, K.L., West, J., and Berner, R.A., 2000, Solute flux and mineral mass balance approaches to the
787 quantification of plant effects on silicate weathering: v. 300, p. 539–570.
- 788 Muñoz, J.A., 1992, Evolution of a continental collision belt: ECORS-Pyrenees crustal balanced cross-section, *in*
789 McClay, K.R. ed., *Thrust Tectonics*, Dordrecht, Springer Netherlands, p. 235–246, doi:10.1007/978-
790 94-011-3066-0_21.
- 791 Murray, J., and Jagoutz, O., 2024, Palaeozoic cooling modulated by ophiolite weathering through organic
792 carbon preservation: *Nature Geoscience*, v. 17, p. 88–93, doi:10.1038/s41561-023-01342-9.
- 793 Pogge von Strandmann, P.A.E., Cosford, L.R., Liu, C.-Y., Liu, X., Krause, A.J., Wilson, D.J., He, X., McCoy-
794 West, A.J., Gislason, S.R., and Burton, K.W., 2023, Assessing hydrological controls on the lithium
795 isotope weathering tracer: *Chemical Geology*, v. 642, p. 121801, doi:10.1016/j.chemgeo.2023.121801.
- 796 Pogge Von Strandmann, P.A.E., Fraser, W.T., Hammond, S.J., Tarbuck, G., Wood, I.G., Oelkers, E.H., and
797 Murphy, M.J., 2019, Experimental determination of Li isotope behaviour during basalt weathering:
798 *Chemical Geology*, v. 517, p. 34–43, doi:10.1016/j.chemgeo.2019.04.020.
- 799 Pogge von Strandmann, P.A.E., Jenkyns, H.C., and Woodfine, R.G., 2013, Lithium isotope evidence for
800 enhanced weathering during Oceanic Anoxic Event 2: *Nature Geoscience*, v. 6, p. 668–672,
801 doi:10.1038/ngeo1875.
- 802 Pogge von Strandmann, P.A.E., Jones, M.T., West, A.J., Murphy, M.J., Stokke, E.W., Tarbuck, G., Wilson,
803 D.J., Pearce, C.R., and Schmidt, D.N., 2021, Lithium isotope evidence for enhanced weathering and
804 erosion during the Paleocene-Eocene Thermal Maximum: *Science Advances*, v. 7, p. eabh4224,
805 doi:10.1126/sciadv.abh4224.



- 806 Pogge von Strandmann, P.A.E., Kasemann, S.A., and Wimpenny, J.B., 2020, Lithium and Lithium Isotopes in
807 Earth's Surface Cycles: v. 16, p. 253–258, doi:10.2138/gselements.16.4.253.
- 808 Porder, S., 2019, How Plants Enhance Weathering and How Weathering is Important to Plants: Elements, v. 15,
809 p. 241–246, doi:10.2138/gselements.15.4.241.
- 810 Prieur, M. et al., 2025, Climate Control on Erosion: Evolution of Sediment Flux From Mountainous Catchments
811 During a Global Warming Event, PETM, Southern Pyrenees, Spain: Geophysical Research Letters, v. 52,
812 p. e2024GL112404, doi:10.1029/2024GL112404.
- 813 Prieur, M., Whittaker, A.C., Nuriel, P., Jaimes-Gutierrez, R., Garzanti, E., Roigé, M., Sømme, T.O.,
814 Schlunegger, F., and Castellort, S., 2024, Fingerprinting enhanced floodplain reworking during the
815 Paleocene–Eocene Thermal Maximum in the Southern Pyrenees (Spain): Implications for channel
816 dynamics and carbon burial: Geology, v. 52, p. 651–655, doi:10.1130/G52180.1.
- 817 Puigdefbregas, C., and Souquet, P., 1986, Tecto-sedimentary cycles and depositional sequences of the Mesozoic
818 and Tertiary from the Pyrenees: v. 129, p. 173–203.
- 819 Pujalte, V., Baceta, J.I., and Schmitz, B., 2015, A massive input of coarse-grained siliciclastics in the Pyrenean
820 Basin during the PETM: the missing ingredient in a coeval abrupt change in hydrological regime:
821 Climate of the Past, v. 11, p. 1653–1672, doi:10.5194/cp-11-1653-2015.
- 822 Pujalte, V., and Schmitz, B., 2005, Revisión de la estratigrafía del Grupo Tremp («Garumniense», Cuenca de
823 Tremp-Graus, Pirineos meridionales):
- 824 Pujalte, V., Schmitz, B., and Baceta, J.I., 2014, Sea-level changes across the Paleocene–Eocene interval in the
825 Spanish Pyrenees, and their possible relationship with North Atlantic magmatism: Palaeogeography,
826 Palaeoclimatology, Palaeoecology, v. 393, p. 45–60, doi:10.1016/j.palaeo.2013.10.016.
- 827 Pujalte, V., Schmitz, B., Baceta, J.I., Orue-Etxebarria, X., Bernaola, G., Dinarès-Turell, J., Payros, A.,
828 Apellaniz, E., and Caballero, F., 2009, Correlation of the Thanetian-Ilerdian turnover of larger
829 foraminifera and the Paleocene-Eocene thermal maximum: confirming evidence from the Campo area
830 (Pyrenees, Spain): Geologica Acta, v. 7.
- 831 Ramos, E.J. et al., 2024, Competition or collaboration: Clay formation sets the relationship between silicate
832 weathering and organic carbon burial in soil: Earth and Planetary Science Letters, v. 628, p. 118584,
833 doi:10.1016/j.epsl.2024.118584.
- 834 Ramos, E.J. et al., 2022, Swift Weathering Response on Floodplains During the Paleocene-Eocene Thermal
835 Maximum: Geophysical Research Letters, v. 49, doi:10.1029/2021GL097436.
- 836 Raymo, M.E., and Ruddiman, W.F., 1992, Tectonic forcing of late Cenozoic climate: Nature, v. 359, p. 117–
837 122, doi:10.1038/359117a0.
- 838 Riebe, C.S., Kirchner, J.W., and Finkel, R.C., 2004, Erosional and climatic effects on long-term chemical
839 weathering rates in granitic landscapes spanning diverse climate regimes: Earth and Planetary Science
840 Letters, v. 224, p. 547–562, doi:10.1016/j.epsl.2004.05.019.
- 841 Roest, W.R., and Srivastava, S.P., 1991, Kinematics of the plate boundaries between Eurasia, Iberia, and Africa
842 in the North Atlantic from the Late Cretaceous to the present: Geology, v. 19, p. 613,
843 doi:10.1130/0091-7613(1991)019<0613:KOTPB>2.3.CO;2.
- 844 Rosenbaum, G., Lister, G.S., and Duboz, C., 2002, Reconstruction of the tectonic evolution of the western
845 Mediterranean since the Oligocene: Journal of the Virtual Explorer, v. 08,
846 doi:10.3809/jvirtex.2002.00053.
- 847 Roure, F., Choukroune, P., Berastegui, X., Munoz, J.A., Villien, A., Matheron, P., Bareyt, M., Seguret, M.,
848 Camara, P., and Deramond, J., 1989, Eors deep seismic data and balanced cross sections: Geometric
849 constraints on the evolution of the Pyrenees: Tectonics, v. 8, p. 41–50, doi:10.1029/TC008i001p00041.



- 850 Rush, W.D., Kiehl, J.T., Shields, C.A., and Zachos, J.C., 2021, Increased frequency of extreme precipitation
851 events in the North Atlantic during the PETM: Observations and theory: *Palaeogeography,*
852 *Palaeoclimatology, Palaeoecology*, v. 568, p. 110289, doi:10.1016/j.palaeo.2021.110289.
- 853 Schmitz, B., and Pujalte, V., 2007, Abrupt increase in seasonal extreme precipitation at the Paleocene-Eocene
854 boundary: *Geology*, v. 35, p. 215, doi:10.1130/G23261A.1.
- 855 Schmitz, B., and Pujalte, V., 2003, Sea-level, humidity, and land-erosion records across the initial Eocene
856 thermal maximum from a continental-marine transect in northern Spain: *Geology*, v. 31, p. 689,
857 doi:10.1130/G19527.1.
- 858 Schmitz, B., Pujalte, V., and Nunhez-Betelu, K., 2001, Climate and sea-level perturbations during the Initial
859 Eocene Thermal Maximum: evidence from siliciclastic units in the Basque Basin (Ermua, Zumaia and
860 Trabakua Pass), northern Spain: *Palaeogeography, Palaeoclimatology, Palaeoecology* 165, p. 299–320.
- 861 Spangenberg, J.E., 2006, Hydrocarbon Biomarkers in the Topla-Mezica Zinc-Lead Deposits, Northern
862 Karavanke/Drau Range, Slovenia: Paleoenvironment at the Site of Ore Formation:
- 863 Spangenberg, J.E., and Zufferey, V., 2019, Carbon isotope compositions of whole wine, wine solid residue, and
864 wine ethanol, determined by EA/IRMS and GC/C/IRMS, can record the wine water status—a
865 comparative reappraisal: *Analytical and Bioanalytical Chemistry*, v. 411, p. 2031–2043,
866 doi:10.1007/s00216-019-01625-4.
- 867 Tanaka, T. et al., 2000, JNd-1: a neodymium isotopic reference in consistency with LaJolla neodymium:
868 *Chemical Geology*, v. 168, p. 279–281, doi:10.1016/S0009-2541(00)00198-4.
- 869 Teixell, A., Labaume, P., and Lagabrielle, Y., 2016, The crustal evolution of the west-central Pyrenees revisited:
870 Inferences from a new kinematic scenario: *Comptes Rendus. Géoscience*, v. 348, p. 257–267,
871 doi:10.1016/j.crte.2015.10.010.
- 872 Tofelde, S., Bernhardt, A., Guerit, L., and Romans, B.W., 2021, Times Associated With Source-to-Sink
873 Propagation of Environmental Signals During Landscape Transience: *Frontiers in Earth Science*, v. 9,
874 p. 628315, doi:10.3389/feart.2021.628315.
- 875 Tremblin, M. et al., 2022, Mercury enrichments of the Pyrenean foreland basins sediments support enhanced
876 volcanism during the Paleocene-Eocene thermal maximum (PETM): *Global and Planetary Change*, v.
877 212, p. 103794, doi:10.1016/j.gloplacha.2022.103794.
- 878 Velde, B., and Meunier, A., 2008, *The Origin of Clay Minerals in Soils and Weathered Rocks*: Berlin,
879 Heidelberg, Springer Berlin Heidelberg, doi:10.1007/978-3-540-75634-7.
- 880 Vigier, N., Decarreau, A., Millot, R., Carignan, J., Petit, S., and France-Lanord, C., 2008, Quantifying Li
881 isotope fractionation during smectite formation and implications for the Li cycle: *Geochimica et*
882 *Cosmochimica Acta*, v. 72, p. 780–792, doi:10.1016/j.gca.2007.11.011.
- 883 Vimperc, L. et al., 2023, Carbon isotope and biostratigraphic evidence for an expanded Paleocene–Eocene
884 Thermal Maximum sedimentary record in the deep Gulf of Mexico: *Geology*, doi:10.1130/G50641.1.
- 885 Walker, J.C.G., Hays, P.B., and Kasting, J.F., 1981, A negative feedback mechanism for the long-term
886 stabilization of Earth's surface temperature: *Journal of Geophysical Research: Oceans*, v. 86, p. 9776–
887 9782, doi:10.1029/JC086iC10p09776.
- 888 Weis, D., Kieffer, B., Maerschalk, C., Pretorius, W., and Barling, J., 2005, High-precision Pb-Sr-Nd-Hf isotopic
889 characterization of USGS BHVO-1 and BHVO-2 reference materials: *Geochemistry, Geophysics,*
890 *Geosystems*, v. 6, p. 2004GC000852, doi:10.1029/2004GC000852.
- 891 West, A., Galy, A., and Bickle, M., 2005, Tectonic and climatic controls on silicate weathering: *Earth and*
892 *Planetary Science Letters*, v. 235, p. 211–228, doi:10.1016/j.epsl.2005.03.020.



- 893 Westerhold, T., Röhl, U., McCarren, H.K., and Zachos, J.C., 2009, Latest on the absolute age of the Paleocene–
894 Eocene Thermal Maximum (PETM): New insights from exact stratigraphic position of key ash layers
895 +19 and –17: *Earth and Planetary Science Letters*, v. 287, p. 412–419, doi:10.1016/j.epsl.2009.08.027.
- 896 Wilson, D.J., Pogge von Strandmann, P.A.E., White, J., Tarbuck, G., Marca, A.D., Atkinson, T.C., and Hopley,
897 P.J., 2021, Seasonal variability in silicate weathering signatures recorded by Li isotopes in cave drip-
898 waters: *Geochimica et Cosmochimica Acta*, v. 312, p. 194–216, doi:10.1016/j.gca.2021.07.006.
- 899 Zachos, J.C., Dickens, G.R., and Zeebe, R.E., 2008, An early Cenozoic perspective on greenhouse warming and
900 carbon-cycle dynamics: *Nature*, v. 451, p. 279–283, doi:10.1038/nature06588.
- 901 Zachos, J.C., Wara, M.W., Bohaty, S., Delaney, M.L., Petrizzo, M.R., Brill, A., Bralower, T.J., and Premoli-
902 Silva, I., 2003, A Transient Rise in Tropical Sea Surface Temperature During the Paleocene-Eocene
903 Thermal Maximum: *Science*, v. 302, p. 1551–1554, doi:10.1126/science.1090110.
- 904 Zeebe, R.E., Ridgwell, A., and Zachos, J.C., 2016, Anthropogenic carbon release rate unprecedented during the
905 past 66 million years: *Nature Geoscience*, v. 9, p. 325–329, doi:10.1038/ngeo2681.
- 906 Zhang, F., Dellinger, M., Hilton, R.G., Yu, J., Allen, M.B., Densmore, A.L., Sun, H., and Jin, Z., 2022,
907 Hydrological control of river and seawater lithium isotopes: *Nature Communications*, v. 13, p. 3359,
908 doi:10.1038/s41467-022-31076-y.
- 909